Materials Today Advances 8 (2020) 100112

Contents lists available at ScienceDirect

Materials Today Advances

journal homepage: www.journals.elsevier.com/materials-today-advances/

Tailorable Fe nanostructures and magnetic anisotropy in $(La_{0.5}Sr_{0.5}FeO_3)_{1-x}$:$Fe_x$ thin films integrated on $SrTiO_3$ and silicon substrates

M. Kalaswad [a], B. Zhang [a], Han Wang [b], X. Wang [b], J. Huang [b], H. Wang [a, b, *]

[a] School of Electrical and Computer Engineering, Purdue University, West Lafayette, IN, 47907, USA
[b] School of Materials Engineering, Purdue University, West Lafayette, IN, 47907, USA

ARTICLE INFO

Article history:
Received 25 June 2020
Received in revised form
22 August 2020
Accepted 25 August 2020
Available online 29 September 2020

Keywords:
Oxide-metal nanocomposite
Vertically aligned nanocomposites
Ferromagnetic anisotropy
Silicon integration

ABSTRACT

Vertically aligned magnetic nanostructures embedded in oxide matrices are an attractive framework for exploring anisotropic properties with potential applications in devices such as magnetic tunnel junctions. Magnetic response can easily be tuned through the growth of self-assembled ferromagnetic nanostructures in oxide-metal nanocomposite thin films. Here, oxide-metal $(La_{0.5}Sr_{0.5}FeO_3)_{1-x}$:$Fe_x$ ($LSFO_{1-x}$:Fe_x) nanocomposite thin films with various molar concentrations of Fe (x = 0.3, 0.4, 0.5) are grown by pulsed laser deposition under reducing conditions. The morphology and magnetic properties of Fe nanostructures are investigated to demonstrate tailorable magnetic anisotropic properties. Increasing the concentration of Fe in the nanocomposites has been found to reduce the aspect ratio of Fe nanostructures thus leading to a lower magnetic anisotropy. In addition, $LSFO_{0.7}$:$Fe_{0.3}$ thin films are successfully integrated on silicon substrates, which is a critical step toward realizing the proposed device applications. This study demonstrates oxide-metal $LSFO_{1-x}$:Fe_x nanocomposites as a unique platform for tailoring magnetic properties and future integration of magnetic nanostructures with tunable magnetic anisotropy for device applications.

1. Introduction

Anisotropic magnetic materials are widely studied for new-generation spin-dependent devices that couple electron spin, charge, and magnetic moments [1–3]. Spintronic devices such as magnetic tunnel junctions (MTJs) present great promises owing to their large device densities, low power consumption, and high thermal stability [4,5]. These qualities make MTJs compelling candidates for use in magnetic memory storage [6–8] and sensors [9–11]. Magnetic anisotropy in these devices is critical for switching the ferromagnetic layers to create low- and high-resistance states. Many efforts have focused on tuning magnetic anisotropy in thin films, typically by the incorporation of seed layers [12], buffer layers [13], or cap layers [14,15].

Compared with the layered approaches, vertically aligned nanocomposites (VANs) offer a simple and attractive approach for tuning magnetic anisotropy, since two-phase materials (e.g., ferromagnetic pillars embedded in a non-ferromagnetic matrix) can be self-assembled in one step. Moreover, VANs have previously shown great capabilities in tuning physical properties such as electrical, optical, and magnetic properties [16–23]. Recently, two-phase VAN systems have been extended from mostly oxide-oxide systems to oxide-metal systems and thus provide much broader material selections for ferromagnetic pillars in the VAN framework. Epitaxial Au [19,24–27], Ni [28,29], and Fe [30–33] nanoparticles and nanopillars in ceramic matrices grown by pulsed laser deposition (PLD) exhibit unique magnetic and optical properties compared with oxide-oxide systems. For example, Huang et al. [29] reported self-assembled Ni nanopillars in a CeO_2 matrix, highlighting magnetic anisotropy for effective magnetic flux pinning centers when integrated on high temperature superconducting $YBa_2Cu_3O_{1-x}$ films. $La_{0.5}Sr_{0.5}FeO_3$:Fe (LSFO:Fe) is one such oxide-metal VAN which consists of self-assembled α-Fe nanowires by the decomposition of $La_{0.5}Sr_{0.5}FeO_3$ into $LaSrFeO_4$ and Fe under reducing conditions [30]. Despite its simple processing method, strong magnetic properties, and promising applications, few studies followed the seminal report. Aside from varying deposition parameters such as laser energy and frequency [31], there have

* Corresponding author.
E-mail address: hwang00@purdue.edu (H. Wang).

https://doi.org/10.1016/j.mtadv.2020.100112

been limited efforts to find the optimal target composition [34] required for the decomposition of $La_{0.5}Sr_{0.5}FeO_3$ into Fe.

In this work, the effects of Fe concentration on the growth morphologies (e.g., Fe nanopillar diameters and aspect ratios) and magnetic properties of $LSFO_{1-x}$:Fe_x (molar ratio x = 0.3, 0.4, and 0.5) thin films are explored. The $LSFO_{1-x}$:Fe_x films with various concentrations of Fe are achieved by adjusting the composition in the composite $(La_{0.5}Sr_{0.5}FeO_3)_{1-y}$:$(Fe_2O_3)_y$ targets (y = 0, 0.06, and 0.12). As shown in the schematics in Fig. 1, the concentration and morphologies of Fe nanostructures are expected to vary with the amount of excess Fe, and thus the magnetic properties such as saturation magnetization and magnetic anisotropy will be tuned. Besides the single crystalline $SrTiO_3$ (STO) substrates, the integration of the $LSFO_{0.7}$:$Fe_{0.3}$ thin films on silicon substrates is also demonstrated as a path toward future practical spintronic devices with Fe-based magnetic nanostructures.

2. Experimental

A pure $La_{0.5}Sr_{0.5}FeO_3$ and two composite targets ($(La_{0.5}Sr_{0.5}FeO_3)_{1-y}$:$(Fe_2O_3)_y$) were prepared using a conventional ceramic sintering method. The two composite targets were made with 6 mol% (y = 0.06) and 12 mol% (y = 0.12) excess Fe_2O_3, compared with the pure $La_{0.5}Sr_{0.5}FeO_3$ target. Epitaxial films were grown on single crystal STO (001) substrates by PLD (KrF excimer laser, λ = 248 nm) with a laser fluence of 1.9 J/cm^2 and laser frequency of 2 Hz, at a growth temperature of 750 °C and under high vacuum. A general overview of the processing method (targets and thin films) is presented in Fig. 1. After deposition, the samples were cooled to room temperature under high vacuum. The films integrated on silicon were grown with the pure $La_{0.5}Sr_{0.5}FeO_3$ target on STO/TiN buffered silicon substrates using the same deposition parameters. Film thicknesses were kept around 100–120 nm. The film morphology was studied using transmission electron microscopy (TEM) and scanning TEM (STEM) with energy-dispersive X-ray spectroscopy (EDS) (FEI TALOS T200X). The detailed TEM and STEM image analyses were also used to calculate the Fe volume densities which were then converted to the atomic ratio of the films. Phase identification and epitaxial quality of the films was characterized by X-ray diffraction (XRD) (PANalytical Empyrean). Magnetic property measurements were performed at 300 K using vibrational sample magnetometry and a superconducting quantum interference device (Quantum Design MPMS 3). A maximum magnetic field of 5000 Oe was applied perpendicular and parallel to the film plane for out-of-plane and in-plane measurements, respectively.

3. Results and discussion

A set of plan-view and cross-sectional TEM images, shown in Fig. 2, were collected for the $LSFO_{0.6}$:$Fe_{0.4}$ thin film sample deposited using the 6 mol% Fe-doped composite target. The results confirm the presence of dark-contrast Fe nanostructures within the bright-contrast LSFO matrix. A low-magnification plan-view image in Fig. 2a shows a distribution of Fe nanoinclusions throughout the view area. Furthermore, the Fe particles have diameters averaged around 8 nm. In Fig. 2b, the high-magnification plan-view TEM image of one representative Fe nanoinclusion reveals a distinct interface between the nanoinclusion and the matrix. Fast-Fourier transform analysis of a region inside the nanoinclusion, shown in Fig. S1, indicates an average d-spacing of 1.98 Å, which is similar to the theoretical value of 2.03 Å for the (110) interplanar spacing of α-Fe. This analysis confirms the presence of Fe (110) nanoinclusions, as reported in previous LSFO-Fe studies [30,31]. The separation of the pure Fe phase from the LSFO matrix indicates at least partial decomposition of the $La_{0.5}Sr_{0.5}FeO_3$ precursor, in accordance with the reaction $2La_{0.5}Sr_{0.5}FeO_3 \rightarrow LaSrFeO_4 + Fe + O_2$ [30]. To explore

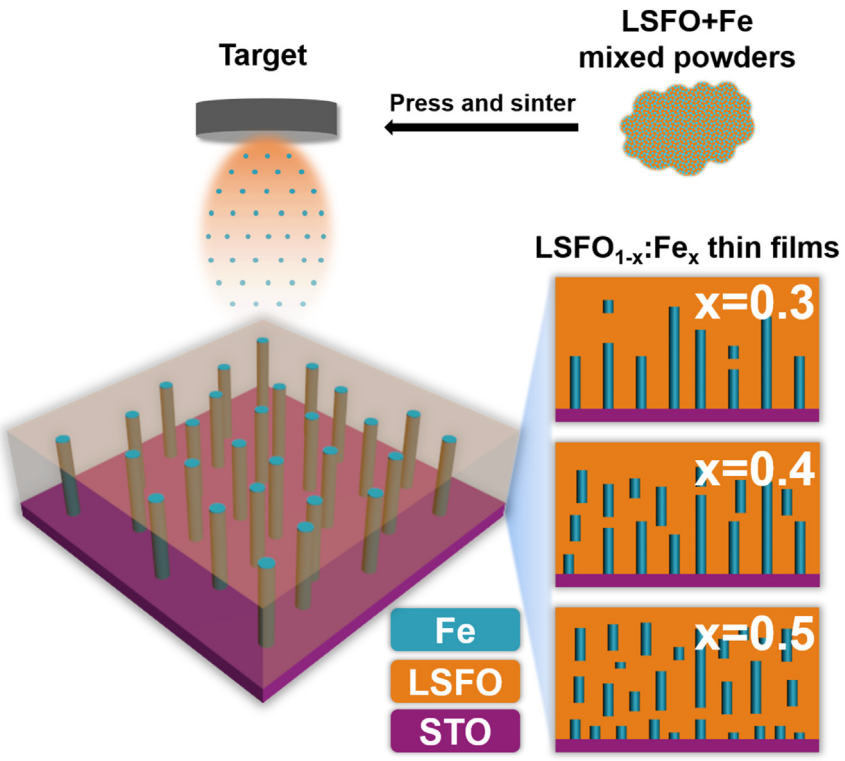

Fig. 1. General overview of the target preparation and subsequent laser ablation to produce $LSFO_{1-x}$:Fe_x vertically aligned nanocomposite thin films. Representative morphologies of the thin films grown with various amounts of Fe are illustrated in the bottom schematics.

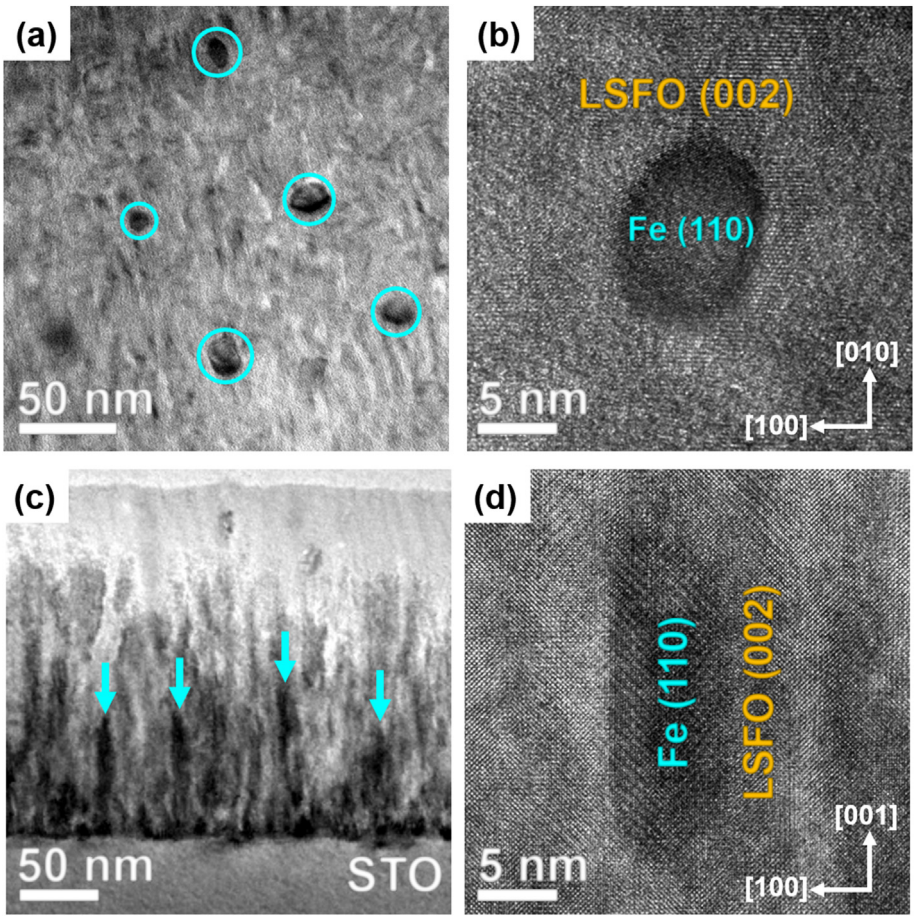

Fig. 2. TEM images of the $LSFO_{0.6}$:$Fe_{0.4}$ film grown on STO (001) substrate, with outlined Fe nanostructures. Plan-view **(a)** low-magnification and **(b)** high-resolution TEM images along with the cross-sectional **(c)** low-magnification and **(d)** high-resolution images clearly indicate the Fe nanopillar structures. STO, $SrTiO_3$; TEM, transmission electron microscopy.

the 3D nature of the Fe nanoinclusions, a cross-sectional TEM study was conducted and the results are shown in Fig. 2c, d. The low-magnification TEM image in Fig. 2c demonstrates the vertical growth of Fe nanopillars with darker contrast within the LSFO matrix with lighter contrast. The nanopillar structures vary slightly in height and do not propagate throughout the entire film thickness. A high-resolution TEM image in Fig. 2d highlights the epitaxial quality of the Fe nanopillar with a diameter of 8 nm, which is consistent with the plan-view image.

The morphology of the $LSFO_{1-x}$:Fe_x samples was further explored using STEM coupled with EDS elemental mapping. Elemental maps of Fe and La are shown in Fig. 3, with the top, middle, and bottom rows corresponding to the samples with Fe proportions of $x = 0.3$, 0.4, and 0.5, respectively. Fe-rich regions in Fig. 3a–c correspond well with La-deficient regions in Fig. 3d–f, providing additional evidence for the separation of the two phases. A thin seed layer of Fe particles can also be seen at the film-substrate interface of all three samples. This layer is formed during the initial stages of deposition, when the surface energy effects are primarily along the lateral (film-substrate) direction. As a result, the Fe particles initially nucleate as nanoparticles rather than pillar-like structures. However, as the deposition continues and the film becomes thicker, the Fe nanoinclusions are able to relax their strain along the vertical direction, leading to the formation of nanopillars. This phenomenon of the interfacial metallic seed layer has also been observed in other oxide-metal VAN systems [27]. Pillar sizes were quantified to determine the average diameters and relative height distributions for each of the compositions. The diameter of Fe nanostructures remains constant at around 8 nm for all three films, which is in agreement with the previously acquired TEM images. The height of the nanopillars, however, tends to decrease with increasing Fe concentration. A possible explanation for this phenomenon is that at higher Fe concentrations, Fe species seek to minimize surface energy, resulting in shorter nanorods. As a result, the number of Fe inclusions increases due to higher doping concentration and shorter nanorods. These trends are made apparent in Fig. 3g–i, which depict the histograms of Fe nanostructure diameters and heights for each of the film compositions. Interestingly, the diameters of the Fe inclusions remain independent of the Fe concentration, possibly because of the strain constraint along the lateral direction from the LSFO matrix. Based on the plan-view and cross-sectional TEM/STEM/EDS images of all three samples, the volume fraction of Fe in the oxide matrix was estimated and from this the molar ratios of the $LSFO_{1-x}$:Fe_x films were calculated. A summary of these values is presented in Table 1. Overall, with increasing Fe concentration, a shift from longer nanopillars to shorter nanorods is evident, and the number of Fe inclusions also increases.

XRD θ-2θ patterns, shown in Fig. 4, were collected to confirm the phases and crystallinity of the $LSFO_{1-x}$:Fe_x thin films grown on STO (001) substrates. In Fig. 4a, LSFO (00*l*) diffraction peaks are visible, suggesting partial decomposition and highly textured growth on the STO (001) substrates. Fig. 4b is an enlarged view between 40° and 50° to discern the $LaSrFeO_4$ (006), Fe (110), LSFO (002), and STO

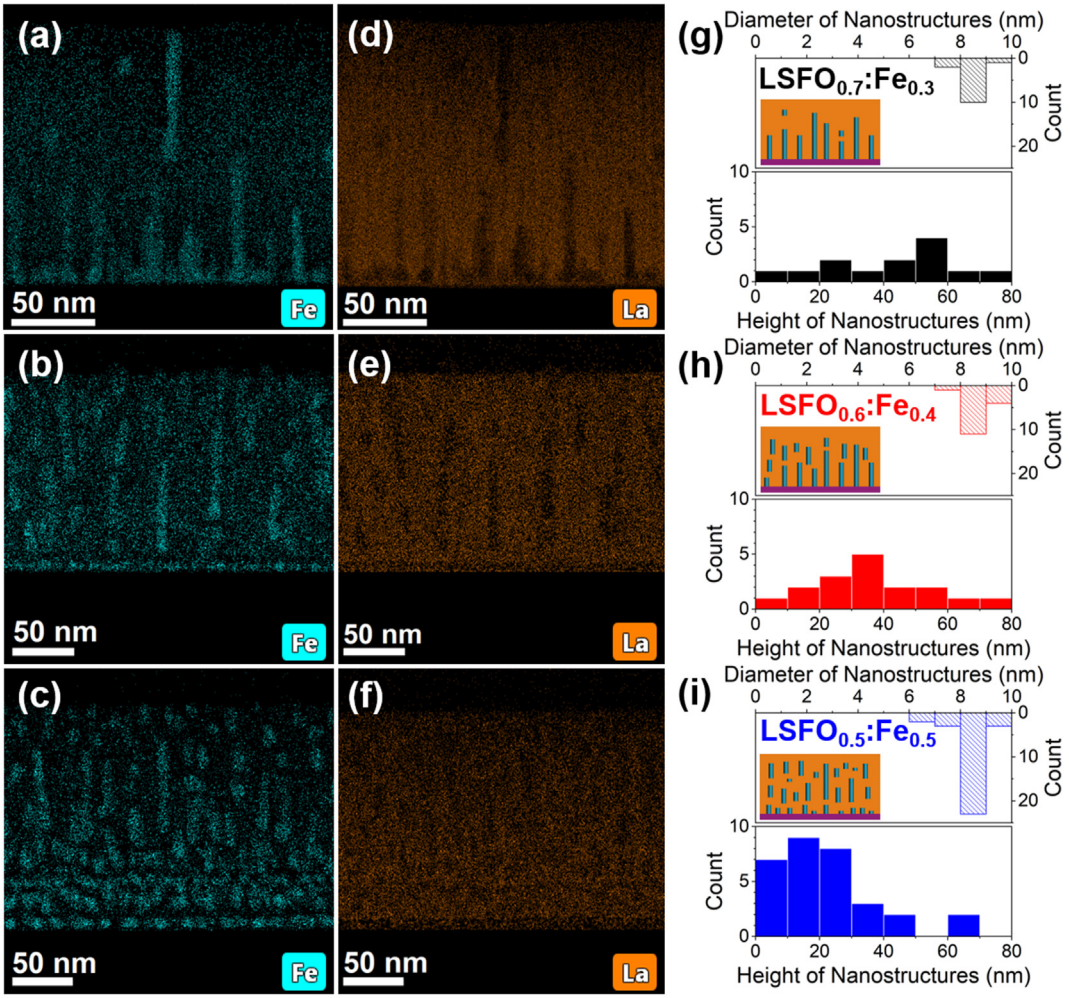

Fig. 3. Microstructure study of $LSFO_{1-x}$:Fe_x films grown with increasing (top to bottom) amounts of Fe. Cross-sectional EDS elemental maps of **(a–c)** Fe and **(d–f)** La, confirming Fe nanostructures within the LSFO matrix. **(g–i)** Diameter and height distributions of Fe nanostructures and inset cartoons recreating observed results. EDS, energy-dispersive X-ray spectroscopy.

Table 1
Summary of target compositions, volume fractions of Fe estimated from TEM/STEM/EDS analyses, and calculated molar ratios of the $LSFO_{1-x}$:Fe_x thin films.

Target composition	Volume fraction of Fe	Film molar ratio
$La_{0.5}Sr_{0.5}FeO_3$	0.15	$LSFO_{0.7}$:$Fe_{0.3}$
$(La_{0.5}Sr_{0.5}FeO_3)_{0.94}$:$(Fe_2O_3)_{0.06}$	0.20	$LSFO_{0.6}$:$Fe_{0.4}$
$(La_{0.5}Sr_{0.5}FeO_3)_{0.88}$:$(Fe_2O_3)_{0.12}$	0.30	$LSFO_{0.5}$:$Fe_{0.5}$

TEM, transmission electron microscopy; STEM, scanning TEM; EDS, energy-dispersive X-ray spectroscopy.

(002) diffraction peaks. The coexistence of LSFO and $LaSrFeO_4$ peaks indicates the decomposition of LSFO into $LaSrFeO_4$ and Fe, with LSFO remaining as the major oxide phase. Although the $LaSrFeO_4$ (006) peak positions remain relatively constant around 42.59°, it is worthwhile to note that the other two peak shifts in this range. The Fe (110) diffraction peak shifts to the right, going from 44.6° to 45.25° with increasing Fe doping concentration. On the other hand, the LSFO (002) peak shifts to the left from 45.95° to 45.25° for increasing Fe concentrations, ultimately overlapping with that of Fe (110). These peak shifts can be explained in terms of the strain coupling between the phases. As more Fe is added to the system, the interface density of Fe nanostructures increases and the strain coupling between Fe and LSFO matrix become more obvious. For example, the 2θ peak of Fe (110) in the $LSFO_{0.7}$:$Fe_{0.3}$ sample matches well with the bulk value of 44.673°, indicating a strain of only −0.153%. When the Fe concentration is increased, the strain increases up to 1.23% (for the $LSFO_{0.5}$:$Fe_{0.5}$ sample). Observations made from XRD measurements couple well with the EDS results described previously, i.e., as the Fe doping concentration increases, the amount of Fe nanostructures in the films increases, and the relative Fe (110) diffraction peak intensity also increases.

To further investigate the relationship between film composition, morphology, and magnetic properties, the magnetization, *M*, of the $LSFO_{1-x}$:Fe_x films as a function of applied magnetic field, *H*, was measured at room temperature. Magnetic anisotropy was determined by applying a magnetic field parallel (in-plane) and perpendicular (out-of-plane) to the surface of the film. *M-H* hysteresis loops presented in Fig. 5a–b demonstrate obvious ferromagnetic behavior for both orientations. These figures show that the magnetic moment saturation, M_S, of the various films increases with increasing Fe doping concentration for both in-plane and out-of-plane orientations. This can be attributed to the fact that there is a higher concentration of ferromagnetic particles (e.g. Fe nano-inclusions) in the films doped with more Fe, leading to higher magnetization. Furthermore, the M_S values for the $LSFO_{1-x}$:Fe_x films measured in the out-of-plane orientation are higher than those

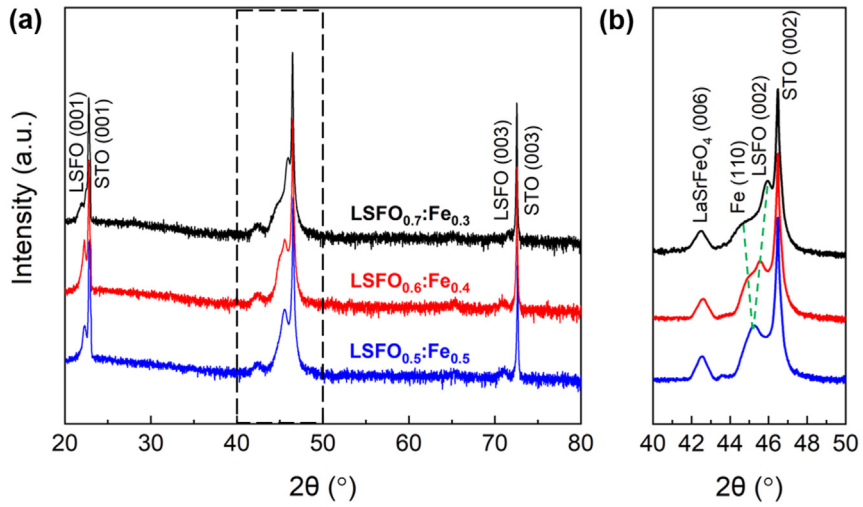

Fig. 4. **(a)** XRD θ-2θ patterns of $LSFO_{1-x}:Fe_x$ thin films grown on STO (001) substrates and **(b)** local area scan centered around Fe (110) to differentiate the neighboring peaks. XRD, X-ray diffraction.

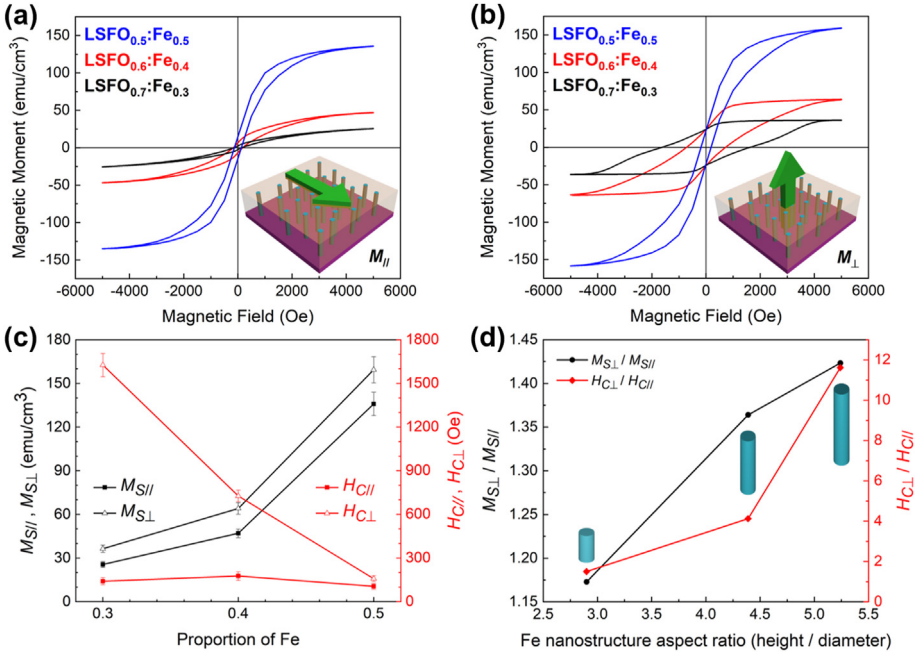

Fig. 5. Room-temperature **(a)** in-plane and **(b)** out-of-plane magnetic hysteresis loops of the $LSFO_{1-x}:Fe_x$ films doped with various concentrations of Fe. **(c)** Plot of saturation magnetization ($M_{S//}$, $M_{S\perp}$) and magnetic coercivity ($H_{C//}$, $H_{C\perp}$) for perpendicular and parallel applied magnetic fields at excess concentrations of Fe. **(d)** Ratios of out-of-plane to in-plane magnetic saturation and coercivity as a function of Fe nanostructure aspect ratio.

measured in the in-plane orientation. This is especially remarkable since the easy axis for Fe is along the in-plane [100] direction, suggesting that the vertical alignment of Fe nanostructures plays a significant role in the magnetic anisotropy. Indeed, the magnetic anisotropy originates from the shape anisotropy of the nanostructured Fe pillars, which have an average aspect ratio (height/diameter) greater than one. These nanopillars are formed by a decomposition process, resulting in columnar Fe domains with a preferred out-of-plane growth orientation. Because of this unique morphology, a stronger out-of-plane magnetization is observed.

The out-of-plane magnetization also shows a dramatic decrease in magnetic coercivity, H_C, with increasing Fe concentration, while the in-plane H_C values remains relatively constant. A decrease in H_C for the out-of-plane orientation can be attributed to shorter Fe nanostructures, whereas the in-plane H_C values are invariant because the nanostructure diameters remain fairly constant. A summary of these trends is shown in Fig. 5c, which are consistent with previous studies on the size of Fe particles in oxide matrices [35,36]. Using the dimensions of the Fe nanostructures in the $LSFO_{1-x}:Fe_x$ thin films, the aspect ratios were calculated and the variation in magnetic anisotropy as a function of the aspect ratio is plotted in Fig. 5d. The anisotropic ratios (out-of-plane/in-plane) of the magnetic saturation and the coercivity are both found to increase with increasing Fe nanostructure aspect ratio. Specifically, the ratio of the out-of-plane to in-plane magnetic moment saturation increases from 1.17 (for the $LSFO_{0.5}:Fe_{0.5}$ film) to 1.42 (for the $LSFO_{0.7}:Fe_{0.3}$ film). Moreover, the magnetic coercivity ratio increases from 1.50 ($LSFO_{0.7}:Fe_{0.3}$) to 11.61 ($LSFO_{0.5}:Fe_{0.5}$). The

pronounced change in the coercivity ratio compared to the magnetic saturation ratio could be due to the relationship between coercivity and particle size, as described in a previous study [36]. Overall, the correlation between the shape anisotropy of the Fe nanostructures and the anisotropic magnetic properties is a good indicator of tailorable anisotropic magnetic properties which can be controlled by Fe doping concentration.

Because of its superior magnetic anisotropy and potential for future magnetic components in devices, the $LSFO_{0.7}$:$Fe_{0.3}$ system was integrated on silicon substrates. To achieve this, a STO/TiN bilayer buffer – which was previously demonstrated for successfully integrating oxide-oxide [17,37] and even oxide-metal [27] VANs on silicon substrates – was first deposited on Si (001) substrates. A 3D schematic of the substrate, buffer layer stack, and $LSFO_{0.7}$:$Fe_{0.3}$ system with Fe nanopillars embedded in the LSFO matrix is shown in Fig. 6a. TiN was selected as a buffer layer material owing to its thermal stability and mechanical integrity. Despite its large lattice mismatch with Si ($f_{TiN\ on\ Si} \approx 24\%$), TiN is capable of cube-on-cube growth on Si (001) through domain matching epitaxy, where four of TiN match well with three of Si [38], as illustrated in Fig. 6b. STO was introduced as an additional buffer layer to further facilitate the growth of the LSFO matrix, since its lattice parameter (a_{STO}= 3.905 Å) is close to that of LSFO (a_{LSFO}= 3.88 Å). The nanostructure of the $LSFO_{0.7}$:$Fe_{0.3}$ film grown on Si (001) was observed from an EDS elemental map, shown in Fig. 6c. Based on their corresponding elements, the TiN and STO buffer layers are clearly visible and well separated, with approximate thicknesses of 10 nm and 30 nm, respectively. Moreover, the morphology of the $LSFO_{0.7}$:$Fe_{0.3}$ film grown on silicon is similar to that grown on STO substrates. Specifically, both samples show an initial Fe seed layer followed by the growth of Fe nanopillars with high anisotropy. Further characterization by XRD reveals the crystallinity of the $LSFO_{0.7}$:$Fe_{0.3}$ film on the bilayer-buffered silicon substrate. The θ-2θ pattern shown in Fig. 6d reveals the $LaSrFeO_4$ (006) and LSFO (002) peaks, indicating the decomposition reaction occurred to form the overall $LSFO_{0.7}$:$Fe_{0.3}$ nanocomposite thin film. Although Fe nanostructures are clearly present in the EDS elemental map, the Fe (110) XRD peak is not visible, possibly due to low intensity, or more likely because it is overlapped with the LSFO (200) peak as was observed in the θ-2θ pattern of the $LSFO_{0.5}$:$Fe_{0.5}$ film grown on the STO substrate. The microstructural characterization by EDS and XRD unambiguously confirms the successful growth of a $LSFO_{0.7}$:$Fe_{0.3}$ thin film on a silicon substrate, and warrants further investigation of the magnetic properties.

The magnetization of the $LSFO_{0.7}$:$Fe_{0.3}$ film grown on Si (001) was measured under the same conditions as the $LSFO_{1-x}$:Fe_x films grown on STO substrates. In-plane and out-of-plane magnetic hysteresis loops obtained at room temperature are shown in Fig. 7. The results clearly indicate ferromagnetic behavior with a stronger response in the out-of-plane orientation, which is likely due to the presence of anisotropic Fe nanostructures in the film. Interestingly, the magnetic saturation for both orientations is comparable, if not greater, for the $LSFO_{0.7}$:$Fe_{0.3}$ film grown on silicon and that grown on the STO substrate. Only the out-of-plane coercivity of the film integrated on silicon is reduced compared with the film grown on STO, which might be due to the height of the Fe nanopillars exceeding the critical value at which coercivity is a maximum. Dimensions greater or less than this value result in decreased coercivity, as previously reported [36]. Overall, the magnetic anisotropy achieved by the $LSFO_{0.7}$:$Fe_{0.3}$ thin film on Si (001) is remarkable and

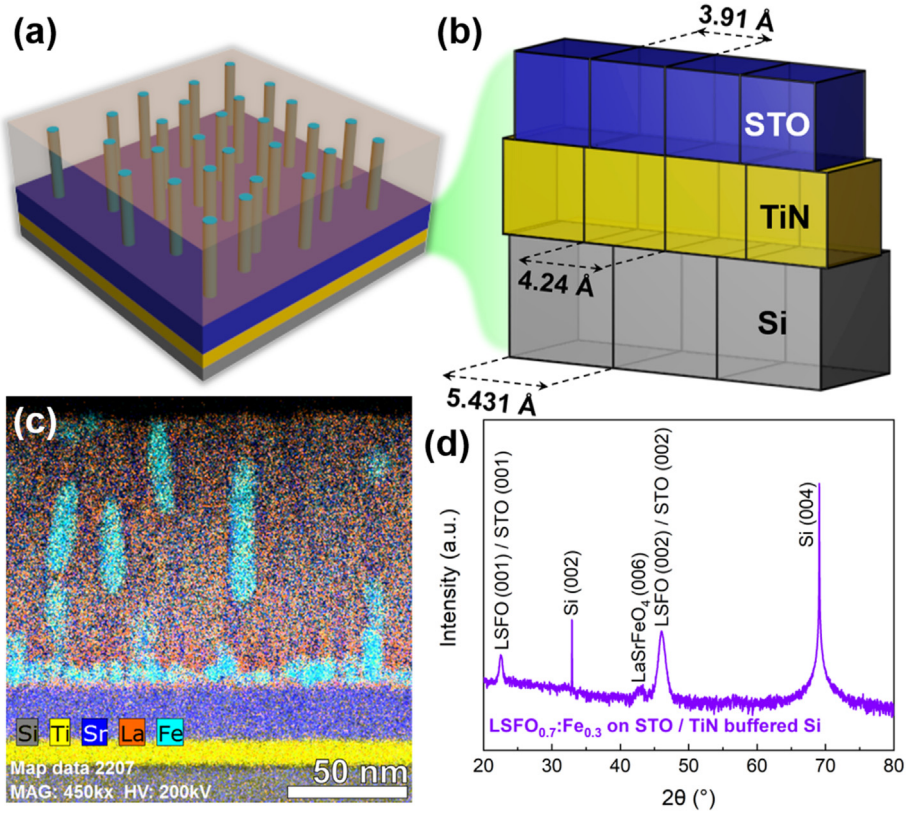

Fig. 6. **(a)** Schematic illustration of the $LSFO_{0.7}$:$Fe_{0.3}$ thin film integrated on STO/TiN bilayer-buffered Si (001) with **(b)** the proposed matching relationship between the bilayer buffer and silicon substrate. **(c)** EDS elemental map highlighting the presence of the buffer layers and Fe nanostructures within the $LSFO_{0.7}$:$Fe_{0.3}$ film. **(d)** XRD θ-2θ pattern of the $LSFO_{0.7}$:$Fe_{0.3}$ film grown on the Si (001) substrate. STO, $SrTiO_3$; EDS, energy-dispersive X-ray spectroscopy; XRD, X-ray diffraction.

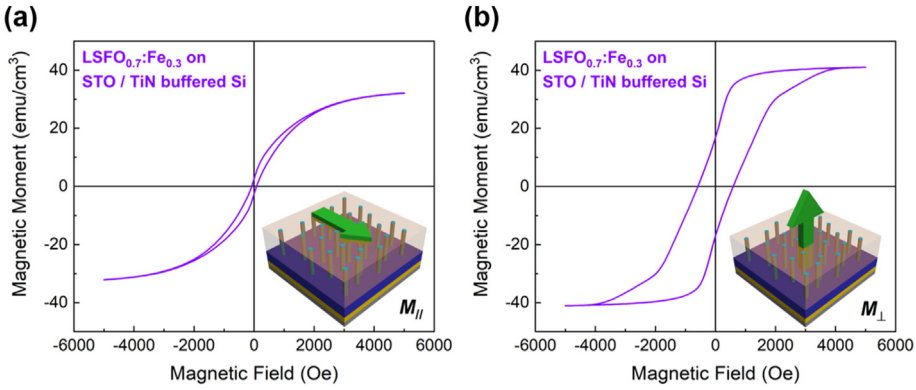

Fig. 7. (**a**) In-plane and (**b**) out-of-plane magnetic hysteresis loops of the $LSFO_{0.7}$:$Fe_{0.3}$ thin film grown on a Si (001) substrate.

opens a new avenue for easy integration of magnetic oxide-metal systems on silicon for MTJs or other spintronic devices.

4. Conclusions

In summary, the effects of Fe doping concentration on the morphology and magnetic properties of the $LSFO_{1-x}$:Fe_x nanocomposite films have been explored by varying the target compositions. By increasing excess Fe concentration, the morphology of the Fe inclusions changed from nanopillars to nanorods and the average aspect ratio of the nanoinclusions reduced from 5.24 to 2.90. As a result, the magnetic properties of $LSFO_{1-x}$:Fe_x thin films were altered. The magnetic anisotropy ratio reduced from 1.42 to 1.17 as Fe concentration increased. Furthermore, higher Fe concentrations created a greater number of Fe nanoinclusions which also increased the saturation magnetization. In short, low Fe doping resulted in samples with Fe nanopillars of high aspect ratio, stronger magnetic anisotropy and coercivity, whereas higher amounts of Fe doping led to samples with nanorods of low aspect ratio and higher saturation magnetization. This work confirms the tailorability of Fe nanostructures in $LSFO_{1-x}$:Fe_x thin films and their anisotropic magnetic properties. The integration of $LSFO_{0.7}$:$Fe_{0.3}$ on a silicon substrate opens up enormous possibilities for future device applications, such as MTJs and high density magnetic data storage.

Data availability

The processed data required to reproduce these findings are available to download from https://doi.org/10.17632/m52425dfmk.2.

Credit author statement

Matias Kalaswad: Investigation, Formal analysis, Visualization, Writing - Original Draft. **Bruce Zhang, Han Wang, Xuejing Wang,** and **Jijie Huang**: Investigation. **Haiyan Wang**: Supervision, Funding acquisition. All authors contributed to Writing - Review & Editing.

Declaration of competing interest

The authors declare that they have no known competing financial interests or personal relationships that could have appeared to influence the work reported in this paper.

Acknowledgements

M.K. and H.W. acknowledge the support from the Basil S. Turner Chair Professorship at Purdue University. M.K. also acknowledges the Purdue Doctoral Fellowship and the U.S. National Science Foundation (AGEP-GRS support under Ceramic Program, DMR-1565822 and the microscopy work DMR-2016453).

Appendix A. Supplementary data

Supplementary data to this article can be found online at https://doi.org/10.1016/j.mtadv.2020.100112.

References

[1] S.A. Wolf, D.D. Awschalom, R.A. Buhrman, J.M. Daughton, S. Von Molnár, M.L. Roukes, A.Y. Chtchelkanova, D.M. Treger, Spintronics: a spin-based electronics vision for the future, Science 294 (2001) 1488–1495, https://doi.org/10.1126/science.1065389 (80-.).
[2] I. Žutić, J. Fabian, S. Das Sarma, Spintronics: fundamentals and applications, Rev. Mod. Phys. 76 (2004) 323–410, https://doi.org/10.1103/RevModPhys.76.323.
[3] D.D. Awschalom, M.E. Flatté, Challenges for semiconductor spintronics, Nat. Phys. 3 (2007) 153–159, https://doi.org/10.1038/nphys551.
[4] N. Nishimura, T. Hirai, A. Koganei, T. Ikeda, K. Okano, Y. Sekiguchi, Y. Osada, Magnetic tunnel junction device with perpendicular magnetization films for high-density magnetic random access memory, J. Appl. Phys. 91 (2002) 5246–5249, https://doi.org/10.1063/1.1459605.
[5] D. Mazumdar, X. Liu, B.D. Schrag, W. Shen, M. Carter, G. Xiao, Thermal stability, sensitivity, and noise characteristics of MgO-based magnetic tunnel junctions (invited), J. Appl. Phys. 101 (2007), https://doi.org/10.1063/1.2710953.
[6] S. Parkin, X. Jiang, C. Kaiser, A. Panchula, K. Roche, M. Samant, Magnetically engineered spintronic sensors and memory, Proc. IEEE 91 (2003) 661–679, https://doi.org/10.1109/JPROC.2003.811807.
[7] S.A. Wolf, J. Lu, M.R. Stan, E. Chen, D.M. Treger, The promise of nanomagnetics and spintronics for future logic and universal memory, in: Proc. IEEE, 2010, pp. 2155–2168, https://doi.org/10.1109/JPROC.2010.2064150.
[8] S.S.P. Parkin, K.P. Roche, M.G. Samant, P.M. Rice, R.B. Beyers, R.E. Scheuerlein, E.J. O'Sullivan, S.L. Brown, J. Bucchigano, D.W. Abraham, Y. Lu, M. Rooks, P.L. Trouilloud, R.A. Wanner, W.J. Gallagher, Exchange-biased magnetic tunnel junctions and application to nonvolatile magnetic random access memory (invited), J. Appl. Phys. 85 (1999) 5828–5833, https://doi.org/10.1063/1.369932.
[9] W. Shen, X. Liu, D. Mazumdar, G. Xiao, In situ detection of single micron-sized magnetic beads using magnetic tunnel junction sensors, Appl. Phys. Lett. 86 (2005) 1–3, https://doi.org/10.1063/1.1952582.
[10] M. Pannetier, C. Fermon, G. Le Goff, J. Simola, E. Kerr, Femtotesla magnetic field measurement with magnetoresistive sensors, Science 304 (2004) 1648–1650, https://doi.org/10.1126/science.1096841 (80-.).
[11] G. He, Y. Zhang, L. Qian, G. Xiao, Q. Zhang, J.C. Santamarina, T.W. Patzek, X. Zhang, PicoTesla magnetic tunneling junction sensors integrated with double staged magnetic flux concentrators, Appl. Phys. Lett. 113 (2018), 242401, https://doi.org/10.1063/1.5052355.
[12] H. Kurt, M. Venkatesan, J.M.D. Coey, Enhanced perpendicular magnetic anisotropy in Co/Ni multilayers with a thin seed layer, J. Appl. Phys. 108 (2010), https://doi.org/10.1063/1.3481452.
[13] D.Y. Lee, S.E. Lee, T.H. Shim, J.G. Park, Tunneling-magnetoresistance ratio comparison of MgO-based perpendicular-magnetic-tunneling-junction spin

valve between top and bottom Co2Fe6B2 free layer structure, Nanoscale Res. Lett. 11 (2016) 1–7, https://doi.org/10.1186/s11671-016-1637-9.
[14] F. Luis, F. Bartolomé, F. Petroff, J. Bartolomé, L.M. García, C. Deranlot, H. Jaffrès, M.J. Martínez, P. Bencok, F. Wilhelm, A. Rogalev, N.B. Brookes, Tuning the magnetic anisotropy of Co nanoparticles by metal capping, Europhys. Lett. 76 (2006) 142–148, https://doi.org/10.1209/epl/i2006-10242-2.
[15] H. Kubota, S. Ishibashi, T. Saruya, T. Nozaki, A. Fukushima, K. Yakushiji, K. Ando, Y. Suzuki, S. Yuasa, Enhancement of perpendicular magnetic anisotropy in FeB free layers using a thin MgO cap layer, J. Appl. Phys. 111 (2012) 1–4, https://doi.org/10.1063/1.3679393.
[16] W. Zhang, L. Li, P. Lu, M. Fan, Q. Su, F. Khatkhatay, A. Chen, Q. Jia, X. Zhang, J.L. MacManus-Driscoll, H. Wang, Perpendicular exchange-biased magneto-transport at the vertical heterointerfaces in La0.7Sr0.3MnO3:NiO nanocomposites, ACS Appl. Mater. Interfaces 7 (2015) 21646–21651, https://doi.org/10.1021/acsami.5b06314.
[17] F. Khatkhatay, A. Chen, J.H. Lee, W. Zhang, H. Abdel-Raziq, H. Wang, Ferroelectric properties of vertically aligned nanostructured BaTiO 3-CeO2 thin films and their integration on silicon, ACS Appl. Mater. Interfaces 5 (2013) 12541–12547, https://doi.org/10.1021/am403834k.
[18] J. Huang, L. Chen, J. Jian, K. Tyler, L. Li, H. Wang, H. Wang, Magnetic (CoFe 2 O 4) 0.1 (CeO 2) 0.9 nanocomposite as effective pinning centers in FeSe 0.1 Te 0.9 thin films, J. Phys. Condens. Matter 28 (2016), 025702, https://doi.org/10.1088/0953-8984/28/2/025702.
[19] L. Li, L. Sun, J.S. Gomez-Diaz, N.L. Hogan, P. Lu, F. Khatkhatay, W. Zhang, J. Jian, J. Huang, Q. Su, M. Fan, C. Jacob, J. Li, X. Zhang, Q. Jia, M. Sheldon, A. Alù, X. Li, H. Wang, Self-assembled epitaxial Au-oxide vertically aligned nanocomposites for nanoscale metamaterials, Nano Lett. 16 (2016) 3936–3943, https://doi.org/10.1021/acs.nanolett.6b01575.
[20] J. Huang, L. Li, P. Lu, Z. Qi, X. Sun, X. Zhang, H. Wang, Self-assembled Co-BaZrO3 nanocomposite thin films with ultra-fine vertically aligned Co nanopillars, Nanoscale 9 (2017) 7970–7976, https://doi.org/10.1039/c7nr01122a.
[21] Q. Su, D. Yoon, Z. Sisman, F. Khatkhatay, Q. Jia, A. Manthiram, H. Wang, Vertically aligned nanocomposite La0.8Sr0.2MnO 3-δ/Zr0.92Y0.08O1.96 thin films as electrode/electrolyte interfacial layer for solid oxide reversible fuel cells, Int. J. Hydrogen Energy 38 (2013) 16320–16327, https://doi.org/10.1016/j.ijhydene.2013.09.128.
[22] J. Huang, J.L. MacManus-Driscoll, H. Wang, New epitaxy paradigm in epitaxial self-assembled oxide vertically aligned nanocomposite thin films, J. Mater. Res. 32 (2017) 4054–4066, https://doi.org/10.1557/jmr.2017.281.
[23] X. Sun, M. Kalaswad, Q. Li, R.L. Paldi, J. Huang, H. Wang, X. Gao, X. Zhang, H. Wang, Role of interlayer in 3D vertically aligned nanocomposite frameworks with tunable magnetotransport properties, Adv. Mater. Interfaces (2020), https://doi.org/10.1002/admi.201901990.
[24] J. Huang, T. Jin, S. Misra, H. Wang, Z. Qi, Y. Dai, X. Sun, L. Li, J. Okkema, H.-T. Chen, P.-T. Lin, X. Zhang, H. Wang, Tailorable optical response of Au-LiNbO 3 hybrid metamaterial thin films for optical waveguide applications, Adv. Opt. Mater. 6 (2018), 1800510, https://doi.org/10.1002/adom.201800510.
[25] S. Misra, L. Li, D. Zhang, J. Jian, Z. Qi, M. Fan, H.T. Chen, X. Zhang, H. Wang, Self-assembled ordered three-phase Au–BaTiO 3 –ZnO vertically aligned nanocomposites achieved by a templating method, Adv. Mater. 31 (2019), 1806529, https://doi.org/10.1002/adma.201806529.
[26] D. Zhang, S. Misra, L. Li, X. Wang, J. Jian, P. Lu, X. Gao, X. Sun, Z. Qi, M. Kalaswad, X. Zhang, H. Wang, Tunable optical properties in self-assembled oxide-metal hybrid thin films via Au-phase geometry control: from nanopillars to nanodisks, Adv. Opt. Mater. 1901359 (2019) 1–10, https://doi.org/10.1002/adom.201901359.
[27] M. Kalaswad, D. Zhang, X. Gao, L. Contreras, H. Wang, X. Wang, H. Wang, Integration of hybrid plasmonic metamaterial on silicon substrates towards Si-based integrated photonics, ACS Appl. Mater. Interfaces 11 (2019) 45199–45206, https://doi.org/10.1021/acsami.9b15528.
[28] Q. Su, W. Zhang, P. Lu, S. Fang, F. Khatkhatay, J. Jian, L. Li, F. Chen, X. Zhang, J.L. Macmanus-Driscoll, A. Chen, Q. Jia, H. Wang, Self-assembled magnetic metallic nanopillars in ceramic matrix with anisotropic magnetic and electrical transport properties, ACS Appl. Mater. Interfaces 8 (2016) 20283–20291, https://doi.org/10.1021/acsami.6b05999.
[29] J. Huang, Z. Qi, L. Li, H. Wang, S. Xue, B. Zhang, X. Zhang, H. Wang, Self-assembled vertically aligned Ni nanopillars in CeO 2 with anisotropic magnetic and transport properties for energy applications, Nanoscale 10 (2018) 17182–17188, https://doi.org/10.1039/c8nr05532g.
[30] L. Mohaddes-Ardabili, H. Zheng, S.B. Ogale, B. Hannoyer, W. Tian, J. Wang, S.E. Lofland, S.R. Shinde, T. Zhao, Y. Jia, L. Salamanca-Riba, D.G. Schlom, M. Wuttig, R. Ramesh, Self-assembled single-crystal ferromagnetic iron nanowires formed by decomposition, Nat. Mater. 3 (2004) 533–538, https://doi.org/10.1038/nmat1162.
[31] B. Zhang, M. Fan, L. Li, J. Jian, J. Huang, H. Wang, M. Kalaswad, H. Wang, Tunable magnetic anisotropy of self-assembled Fe nanostructures within a La0.5Sr0.5FeO3 matrix, Appl. Phys. Lett. 112 (2018), https://doi.org/10.1063/1.5008382, 0–5.
[32] B. Zhang, J. Huang, B.X. Rutherford, P. Liu, S. Misra, M. Kalaswad, L. Li, H. Wang, Tunable, room temperature multiferroic Fe-BaTiO3 vertically aligned nanocomposite with perpendicular magnetic anisotropy, Mater. Today Nano. 11 (Aug 2020) 100083, https://doi.org/10.1016/j.mtnano.2020.100083.
[33] M. Kalaswad, B. Zhang, X. Wang, H. Wang, X. Gao, H. Wang, Integration of highly anisotropic multiferroic BaTiO3–Fe nanocomposite thin films on Si towards device applications, Nanoscale Adv. (2020), https://doi.org/10.1039/d0na00405g. In press.
[34] K. Okada, H. Tanaka, Compositionally tunable three-dimensional nano-seeding assembly in Fe-LaSrFeO4 nanostructure, J. Appl. Phys. 113 (2013), https://doi.org/10.1063/1.4791756.
[35] D. Kumar, J. Narayan, A.V. Kvit, A.K. Sharma, J. Sankar, High coercivity and superparamagnetic behavior of nanocrystalline iron particles in alumina matrix, J. Magn. Magn Mater. 232 (2001) 161–167, https://doi.org/10.1016/S0304-8853(01)00191-3.
[36] D.L. Huber, Synthesis, properties, and applications of iron nanoparticles, Small 1 (2005) 482–501, https://doi.org/10.1002/smll.200500006.
[37] W. Zhang, A. Chen, F. Khatkhatay, C.F. Tsai, Q. Su, L. Jiao, X. Zhang, H. Wang, Integration of self-assembled vertically aligned nanocomposite (La 0.7Sr0.3MnO3)1-x:(ZnO)x thin films on silicon substrates, ACS Appl. Mater. Interfaces 5 (2013) 3995–3999, https://doi.org/10.1021/am400068h.
[38] H. Wang, A. Sharma, A. Kvit, Q. Wei, X. Zhang, C.C. Koch, J. Narayan, Mechanical properties of nanocrystalline and epitaxial TiN films on (100) silicon, J. Mater. Res. 16 (2001) 2733–2738, https://doi.org/10.1557/JMR.2001.0373.